



Heat transfer enhancement of a microchannel heat sink with the combination of impinging jets, dimples, and side outlets

Ting Gan¹ · Tingzhen Ming¹ · Weijie Fang¹ · Yang Liu¹ · Lei Miao¹ · Kun Ren² · Mohammad Hossein Ahmadi³

Received: 4 June 2019 / Accepted: 23 August 2019 / Published online: 12 September 2019
© Akadémiai Kiadó, Budapest, Hungary 2019

Abstract

With the rapid increasing heat fluxes released from micro electronic devices, thermal management of electric components faces huge challenge. High working temperature generated by the chip will directly affect its performance. It is essential to develop advanced model to enhance heat transfer. In this study, a new microchannel heat sinks with impinging jets and dimples (MHSIJD) model with side outlets was proposed. Computational fluid dynamics simulation methodology with RNG $k-\varepsilon$ turbulence model was used to investigate the performance of MHSIJD with side outlets. Valuation indices including thermal capability, pump consumption and overall performance were analyzed. Three models were compared with basic model (MHSIJD without side outlets): the cross section of the side outlet was set as 0.2×0.2 mm (Case 1), 0.4×0.4 mm (Case 2), and 0.6×0.6 mm (Case 3). The results showed that: (1) the MHSIJD with side outlets performs better heat transfer characteristic due to the alleviation of drift phenomenon. The heat transfer capacity can be increased by up to 17.51%; (2) the MHSIJD with side outlets exhibits a lower pressure drop, which can be reduced up to 22.39%; and (3) the overall performance of MHSIJD with side outlets is better due to its higher cooling efficiency and lower pump consumption.

Keywords Microchannel heat sink · Heat transfer enhancement · Side outlet · Impinging jet · Dimple

List of symbols

$C_{1\varepsilon}$	Empirical constants 1.42	H_3	Height of side outlet in cross section (mm)
$C_{2\varepsilon}$	Empirical constants 1.68	h	Convective heat transfer coefficient ($\text{W m}^{-2} \text{K}^{-1}$)
C_μ	Empirical constants 0.085	k	Turbulent kinetic energy
C_p	Isobaric specific heat ($\text{J K}^{-1} \text{kg}^{-1}$)	k_f	Thermal conductivity of the fluid ($\text{W m}^{-1} \text{K}^{-1}$)
f	Acceleration of gravity (m s^{-2})	L	Heat sink length (mm)
G_k	Turbulent kinetic energy caused by the average velocity gradient	L_1	Length of jet in cross section (mm)
H	Heat sink height (mm)	L_2	Spacing between jets (mm)
H_1	Jet height (mm)	\overline{Nu}	Nusselt number (—)
H_2	Channel height (mm)	P	Total pressure (Pa)
		Pr_T	Turbulent Prandtl number
		\hat{q}	Heat flux (W m^{-2})
		R	Radius of dimple (mm)
		Re	Reynolds number (—)
		S	Deformation rate tensor
		t	Time—for unsteady items (s)
		T	Temperature (K)
		u	Velocity (m s^{-1})
		W	Heat sink width (mm)
		W_1	Channel width (mm)
		x, y, z	Cartesian coordinates (—)

✉ Tingzhen Ming
tzming@whut.edu.cn

✉ Lei Miao
leimiao@whut.edu.cn

¹ School of Civil Engineering and Architecture, Wuhan University of Technology, Wuhan 430070, China

² Institute of Electric Power, North China University of Water Resources and Electric Power, No.136 Jinshui East Road, Zhengzhou 450046, China

³ Mechanical Engineering, Shahrood University of Technology, Shahrood, Iran

Greek symbols

α_k Inverse effective Prandtl numbers for k

α_ε	Inverse effective Prandtl numbers for ε
β	Volume coefficient of expansion (1 K^{-1})
δ	Kronecker delta
ε	Turbulent dissipation rate
μ	Dynamic viscosity (Pa s)
μ_t	Turbulent viscosity
τ	Shear stress caused by viscosity (N m^{-2})
ρ	Density (kg m^{-3})
ΔP	Pressure drop (Pa)

Subscripts

f	Fluid
in	Impinging jet inlet
out	Channel outlet
i, j	Any direction of x, y and z
w	Cooled surface
\bar{a}	Time average of a
T	Temperature

Introduction

With an increase in the number of transistors in electronic chips, the heat flux density of a new generation of electrical devices has reached $100\text{--}1000 \text{ W cm}^{-2}$. The reliability of electronic components is closely related to their operating temperature. When the temperature approaches $70\text{--}80 \text{ }^\circ\text{C}$, the reliability declines by 10% for every $2 \text{ }^\circ\text{C}$ increase in temperature [1]. The maximum heat flux density of a heat sink based on fan cooling technology is approximately 100 W cm^{-2} [2]. Traditional heat transfer technology cannot meet cooling requirements [3], as large flux generation places greater demand on the cooling capacity of electronic devices. In 1981, Tuckerman and Pease [4] proposed the concept of microchannel heat sinks (MHS), confirming that water-cooled MHS have a cooling capacity of 790 W cm^{-2} . Since then, many researchers have carried out in-depth research on MHS. Recently, most of studies have focused on analyzing structural changes [5, 6], different working fluids [7–10], and the effects of their combination [11–13], which have a great impact on heat dissipation [14–16].

MHS with different channel structures demonstrate different heat diffusion effects [17–19]. There have been many articles comparing the heat transfer performance of microchannels with different cross-sectional shapes, but inconsistent conclusions have been drawn. Chen et al. [20] pointed out that the triangular channel has the best cooling efficiency, followed by the trapezoidal channel, whereas the rectangular channel shows the worst heat transfer characteristics. However, the rectangular channel was

found to be better than a triangular or trapezoidal channel in terms of heat transfer [21]. Wang et al. [22] further investigated the influence of the cross-sectional shapes and aspect ratios of microchannels on heat transfer by keeping the cross-sectional areas unchanged. Numerical results indicated that the minimum thermal resistance was accompanied by a rectangular cross section, whereas the triangular cross section exhibited maximum thermal resistance. A rectangular microchannel with a higher aspect ratio usually demonstrated lower thermal resistance within a given cross-sectional area, consistent with the conclusions of Xie et al. [23] and Cao and Chen [24].

In a long, straight, rectangular microchannel, the thermal boundary layer will become thicker along the flow direction, which is a major problem that inhibits heat transfer. Dean vortices can quickly develop along the flow direction and disturb the boundary layer [25], which is beneficial to enhancing heat transfer in a wavy microchannel at a moderate Reynolds number [26]; channels with a wavy top and bottom can provide improved overall thermal performance compared to straight channels [27].

An effective way to enhance heat transfer involves increasing the disturbance, including through the use of impinging jets, pin fins, dimples, vortex generators, and other means. Impinging jets help fluids mix better and thus play a role in reducing boundary layer thickness, which can significantly improve heat transfer [28]. However, if microchannel heat sinks with impinging jets (MHSMIJ) work under unsteady impinging jets and heat flux, the thermal fatigue phenomenon can easily follow and shorten the longevity of MHSMIJ [29]. The flow and heat transfer performance of different jet microchannels (MIJ) have been studied through experiments and numerical simulations [30–32]. Results indicate that the velocity of jet fluid exerts a great influence on heat transfer performance. When the jet velocity is small, heat dissipation of the microchannel is dominant; at a high velocity, however, the heat dissipation effect of the jet is dominant. Moreover, the critical heat flux density of a heat sink can also influence subcooling of the cooling medium. A water-cooled impinging jet microchannel radiator increases the pressure drop caused by impact to enhance heat transfer. Under certain conditions, MIJ with air as a working medium performs better than water [33]. The model's cooling efficiency is 48.5% higher than the microchannel using water, and the pressure drop is reduced by 90.5%.

Pin fins are regarded as an excellent spoiler for high thermal conductivity and play an important role in heat transfer enhancement [34, 35]. Although different structural parameters [36–38], alignment schemes [37], and tip clearance [39–41] exert distinct influences on heat transfer and flow characteristics, they can all increase heat

diffusivity compared to the smooth wall. However, pin fins cause a large pressure drop. Excessive pumping power consumption owing to flow blockage will affect heat transfer performance [42]. The specific surface area of the dimple is always smaller than that of the pin fin, and the expansion ability on the heat exchange surface is slightly lower. However, there is a smaller retardation effect on the working medium with a relatively smooth surface, which conserves substantial pump power consumption. Studies [43–45] have shown that dimples can boost thermal transmission by disturbing the boundary layer. Microchannel heat sinks using nanofluid [46, 47] or non-Newton [48] fluid have also displayed the same characteristics of heat transfer enhancement.

Microchannel heat sinks with impinging jets and dimples (MHSIJD) that combine three cooling technologies have been found to provide better thermal performance compared with a single cooling technology [49, 50]. Numerical results indicate that MIJ with convex dimples exhibit the best cooling performance, followed by those without dimples, with mixed dimples, and with concave dimples [51]. An increase in the radius or height of dimples is beneficial to heat transfer in MIJ with convex dimples [52, 53]. However, as the upstream jet converges in MIJ, the crossflow gradually strengthens along the flow direction, resulting in a drift phenomenon [54]. The main factor limiting heat transfer enhancement in MHSIJD is crossflow, which hinders downstream impinging jets from coming into direct contact with the cooled surface; this pattern results in nonuniform temperature distribution. The local high temperature caused by the drift phenomenon threatens the operational ability and service life of electronic devices. In the present study, a new MHSIJD structure with side outlets is proposed, named the compared model, to alleviate the drift phenomenon. Some fluid is exhausted from the side outlets so the crossflow has less effect on downstream impinging jets in the new structure. Conversely, the heat transfer surface area is expanded, eliciting enhanced heat transfer between the working fluid and heat sink. Four structures are numerically evaluated in several aspects: heat exchange, pressure drop, and overall performance. Results indicate that MHSIJD with side outlets can lead to higher heat transfer efficiency and a lower pressure drop than other models.

Model description

Geometric model

Figure 1 presents the integral compared model. Twelve impinging holes are uniformly distributed on the microchannel ceiling, with nozzles facing the convex

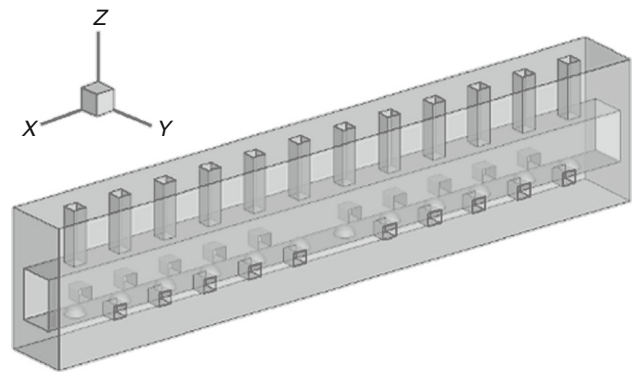


Fig. 1 Overall geometric model of MHSIJD with side outlets

dimples with a radius R . The heat of the chip is conducted to the microchannel via the heat sink below the channel. A series of outlets are provided at the side wall of channel, in the center of adjacent dimples except at the most intermediate position. Water is injected through the impinging holes and acts as a cooling medium. Both ends of the channel are the main outlets. After the cooling water flows through the hemispherical dimples, some of the fluid flows out from the side outlets, and the rest flows in the channel direction to the main outlet.

Given that the microchannel and dimples along the X and Y axes are symmetric, 1/4 of the overall model was simulated to reduce calculation costs. The external faces of the model are assumed to be adiabatic in this study. Four outlets of different lengths were studied: 0 mm (basic model), 0.2 mm (Case 1), 0.4 mm (Case 2), and 0.6 mm (Case 3). The MHSIJD with side outlets was compared with MHSIJD without such outlets, called the basic model. The computational model is displayed in Fig. 2.

Figure 3 shows the front view of the side outlets and dimples. The center of the side outlets faces the center of every two adjacent dimples. The lengths of the side outlets are 0 mm, 0.2 mm, 0.4 mm, and 0.6 mm, respectively. In

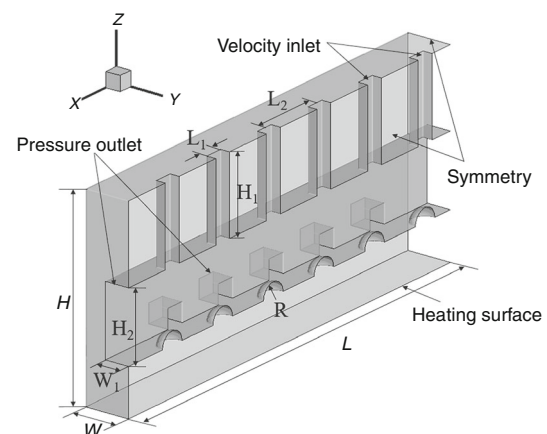


Fig. 2 Computational model of MHSIJD with side outlets

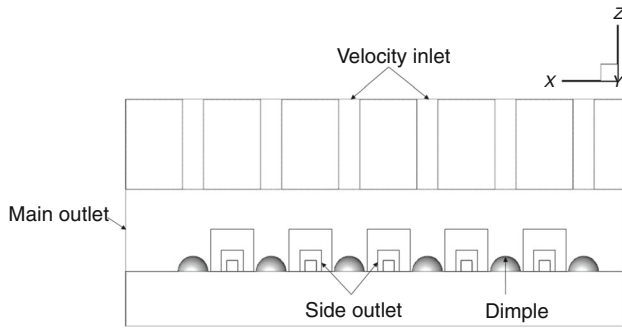


Fig. 3 Side outlets of different sizes

Table 1 Geometric parameters of MHSIJD with side outlets

Parameter/mm	Basic model	Case 1	Case 2	Case 3
L	9.1			
L_1	0.39			
L_2	1.43			
H	4.15			
H_1	1.65			
H_2	1.5			
H_3	0	0.2	0.4	0.6
W	0.92			
W_1	0.5			
R	0.275			

the geometric model, L , W , and H denote the length, width, and height, respectively. The impinging hole is a square with L_1 as the side length, H_1 as the height, and L_2 as the space between impinging holes. The section of side outlets is square with a height H_3 . The width and height of the microchannel are represented by $2W_1$ and H_2 , respectively. Each dimple is a hemisphere with radius R . All geometric parameters are listed in Table 1.

Governing equations

The MHSIJD has a magnitude in the order of millimeters, much larger than the free path of a molecular movement. Therefore, the continuity hypothesis is applied to the computational model, assuming no velocity-slip at the wall. The governing equations of incompressible flow in the microchannel model are as follows:

Continuity equation:

$$\frac{\partial \bar{u}_i}{\partial x_i} = 0 \tag{1}$$

Momentum equation:

$$\frac{\partial \bar{u}_i}{\partial t} + \bar{u}_j \frac{\partial \bar{u}_i}{\partial x_j} = \bar{f}_i - \frac{1}{\rho} \frac{\partial \bar{p}}{\partial x_i} + \frac{1}{\rho} \frac{\partial}{\partial x_j} \left(\bar{\tau}_{ij} - \rho \overline{u'_i u'_j} \right) \tag{2}$$

Energy equation:

$$\rho c_p \left[\frac{\partial \bar{T}}{\partial t} + \bar{u}_j \frac{\partial \bar{T}}{\partial x_j} \right] = \frac{\partial}{\partial x_j} \left(k_f \frac{\partial \bar{T}}{\partial x_j} - \rho c_p \overline{u'_j T'} \right) \tag{3}$$

where $-\rho \overline{u'_i u'_j}$ and $-\rho c_p \overline{u'_j T'}$ are caused by turbulent pulsation. RNG $k-\varepsilon$ model are employed for turbulent treatment, and the two terms were calculated as $-\rho \overline{u'_i u'_j} = -\frac{2}{3} \rho k \delta_{ij} + 2\mu_t \overline{S}_{ij}$ and $-\rho c_p \overline{u'_j T'} = \frac{\mu_t c_p}{Pr_T} \frac{\partial \bar{T}}{\partial x_j}$. Where $\mu_t = \rho C_\mu \frac{k^2}{\varepsilon}$ represents turbulent viscosity; k and ε represent the turbulent kinetic energy and turbulent dissipation rate, respectively; τ_{ij} represents shear stress caused by viscosity which is calculated by $\tau_{ij} = 2\mu S_{ij}$; S_{ij} is deformation rate tensor calculated by $S_{ij} = \frac{1}{2} \left(\frac{\partial \bar{u}_i}{\partial x_j} + \frac{\partial \bar{u}_j}{\partial x_i} \right)$; δ_{ij} is Kronecker delta function; Pr_T is turbulent Prandtl number.

Turbulent kinetic equation k :

$$\frac{\partial(\rho k)}{\partial t} + \frac{\partial(\rho k u_i)}{\partial x_i} = \frac{\partial}{\partial x_j} \left(\alpha_k \mu_{\text{eff}} \frac{\partial k}{\partial x_j} \right) + G_k + \rho \varepsilon \tag{4}$$

Turbulent kinetic energy dissipation rate ε :

$$\frac{\partial(\rho \varepsilon)}{\partial t} + \frac{\partial(\rho \varepsilon u_i)}{\partial x_i} = \frac{\partial}{\partial x_j} \left(\alpha_\varepsilon \mu_{\text{eff}} \frac{\partial \varepsilon}{\partial x_j} \right) + \frac{C_{1\varepsilon} \varepsilon}{k} G_k - \left[C_{2\varepsilon} + \frac{\eta(1-\eta/\eta_0)}{1+\beta\eta^3} \right] \rho \frac{\varepsilon^2}{k} \tag{5}$$

where $\mu_{\text{eff}} = \mu + \mu_t$; α_k and α_ε represent the inverse effective Prandtl numbers for k and ε , respectively, which can be set as 1.39 and 1.39, respectively. G_k denotes the generation of turbulent kinetic energy due to the average velocity gradient; $\eta = \frac{S_{ij} k}{\varepsilon}$, and η_0 was set as 4.38; β is volume coefficient of expansion can be set as 0.012; C_μ , $C_{1\varepsilon}$, and $C_{2\varepsilon}$ are empirical constants which can be set as 0.085, 1.42, and 1.68, respectively.

Boundary conditions

In this simulation, the entrance of impinging holes is set as the inlet boundary with water as the working fluid. A uniform inlet velocity and temperature of 280 K are adopted; the velocity is perpendicular to the inlet surface, and the mass flow is within the range of 1–6 g s⁻¹ under Reynolds number from 213 to 1276. The relative outlet pressure is set at 0 Pa. The Reynolds number is defined as

$$Re = \frac{\rho u_{\text{in}} D}{\mu} \tag{6}$$

where u_{in} is the velocity of the jet inlet. D represents the hydraulic diameter of a impinging jet.

The overall model is symmetrical in the X and Y directions. Symmetry boundary conditions are applied to length and width; that is, the model is halved in the X and Y directions. Both symmetry surfaces are adiabatic, and the velocity gradient is zero. A constant heat flux of

500 W cm^{-2} is applied at the bottom of the heat sink, representing heat distribution from electronic devices. The flow-solid interface is a no-slip surface with equal heat flux on both sides.

Mesh processing

Computational area discretization is a critical step in computational fluid dynamics (CFD). The fluid region includes impinging holes and the microchannel; the mesh result is shown in Fig. 4. To balance the cost, time, and accuracy of computational solutions in CFD, two mesh types are used in this model. Unstructured tetrahedral grids are used in the fluid zone and part of the region close to the channel; hexahedral grids were used in the other domain. The spacing of grids in the water-flow zone is reduced because heat transfer is important in this region.

Computational procedure

The simulation was performed in ANSYS FLUENT 14.0. The microchannel heat sink is composed of red copper with inner turbulence. The standard wall function is used for the near-wall treatment; the RNG $k-\varepsilon$ model is used for the turbulent treatment to simulate flow and heat transfer in the fluid region [55]. The SIMPLE algorithm is applied for pressure-velocity coupling. The discretization scheme is set as second-order upwind. The convergence residual of the energy equation is 10^{-7} and 10^{-5} for other equations.

Verification of mesh independence

To verify grid independence in the calculation, for the basic model, three mesh numbers are tested with a mass flow of 2 g s^{-1} with 2,966,000 meshes, 3,428,000 meshes, and 3,701,000 meshes. As shown in Table 2, the average temperature of the cooled surface is 349.16, 347.56, and 347.54 K, respectively, with a relative error being less than 1%. Therefore, 3,428,000 meshes were chosen for numerical calculations to guarantee sufficiently accurate results.

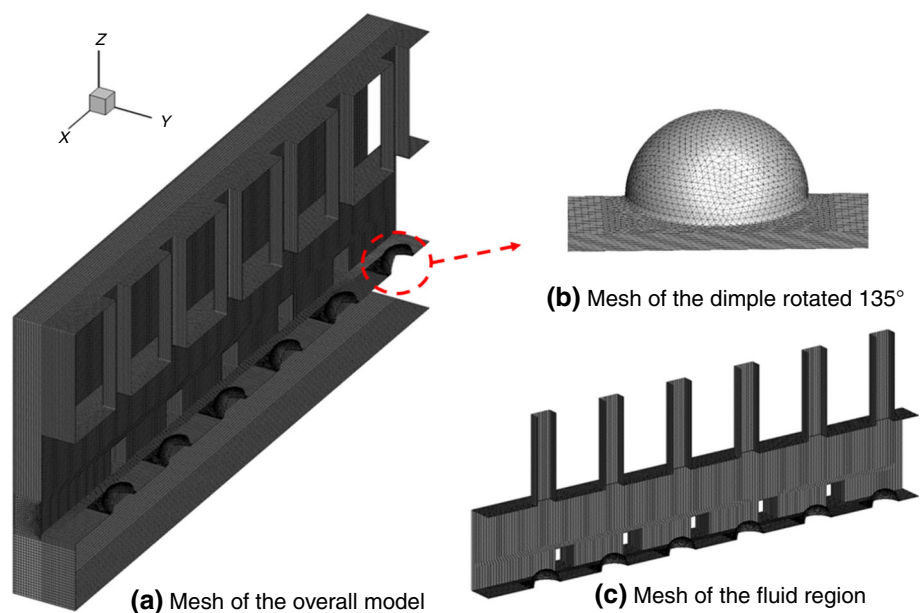
Model validation

To verify the feasibility of RNG $k-\varepsilon$ model, we created a model which was consistent with the experimental geometric specifications in the reference by El-Gabry and Kaminski [56]. Air cooled the target surface at a jet Reynolds numbers (Re) of 15,000 to 35,000, and flow exited in only one direction. A comparison of numerical and experimental data of average Nusselt number (\overline{Nu}) of target surface is plotted in Fig. 5, respectively. A good overall

Table 2 The results of verification of mesh independence

Mesh cells	The average temperature of the cooled surface/K
2,966,000	349.16
3,428,000	347.56
3,701,000	347.54

Fig. 4 Grid system of computational model



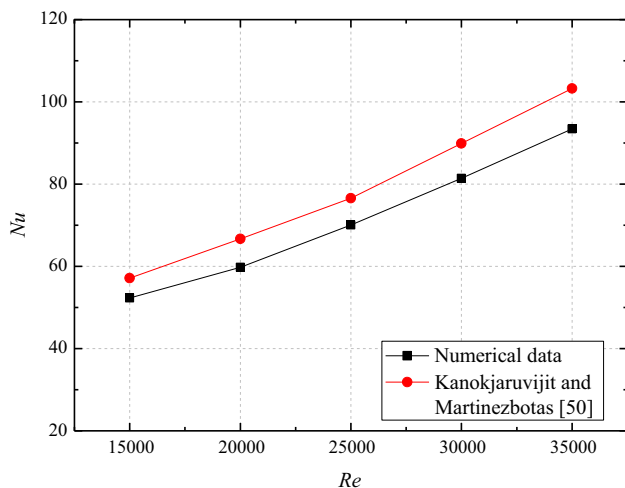


Fig. 5 Comparison of numerical and experimental data in literature of average Nusselt numbers on target surface

agreement is found, and the maximum of relative error is 10.3%. The relative error between simulation results and the experimental data mainly can be attributed to two reasons. On the one hand, due to the inherent limitations of the RANS numerical model, the results can only be obtained based upon the ideal theoretical models. On the other hand, the use of the assumptions, i.e., the adiabatic conditions of the wall surfaces, in numerical calculations may also cause differences between the simulation results and the experimental data.

Results and discussion

To study the effect of the cross-sectional size of side outlets on MHSIJD, we compare different schemes by analyzing heat transfer characteristics, flow resistance, and overall performance, considering flow and heat transfer.

Analysis of heat transfer characteristics

Figure 6 shows the velocity distribution on the symmetry plane of MHSIJD. For the given model and conditions, the flow velocity in the channel gradually increases along the direction of the X axis due to the accumulation of upstream fluid, forming a stronger and stronger crossflow. Along the X direction, as the crossflow becomes stronger, it produces a greater drifting effect on downstream jets. The drift phenomenon is alleviated as the side outlets become larger. For the basic model, the downstream jet near the main outlet directly escapes from the main outlet due to the strong scouring force of the crossflow. This phenomenon is due to fluid discharge from the side outlets; as the side outlets areas increases, the crossflow in the channel

declines, alleviating the deflection effect on jets caused by crossflow. The fullest contact occurs between jets and the cooled surface in Case 3, as shown in Fig. 6.

Figure 7 indicates the temperature distribution on the symmetry plane of MHSIJD. For the given model and conditions, the temperature of the heat sink rises along the X direction for the following reasons. (1) According to the theory of full development of the boundary layer, the thermal boundary layer gradually develops regularly with flow, and the thickness increases. Therefore, the thicker layer downstream hinders heat transfer between the fluid and heat sink, resulting in a higher heat sink temperature downstream. (2) The cooling water upstream becomes warmer after heat exchange with the heat sink, and the heated crossflow and low-temperature jet flow mix as the cooling water flows downstream. Consequently, the cooling efficiency downstream is lower because the cooling water temperature downstream is higher than that upstream.

Figure 7 reveals that with an increase in the side outlets areas, the heat exchange effect downstream is clearly improved, and the temperature difference between upstream and downstream gradually declines. This is because with an increase in the side outlets areas, drift phenomenon is significantly mitigated. Downstream impinging jets can contact with cooled surface well, which lead to smaller discrepancy of temperature on cooled surface upstream and downstream. As shown in Fig. 7, with an increase in the side outlets areas, it is clear that the overall trend of the isotherm between cooled surface and heated surface becomes more and more gradual, which means the temperature difference between upstream and downstream gradually declines.

Figure 8 depicts the average temperature on the cooled surface; that of the compared model is substantially lower than in the basic model for three reasons. (1) The inner surfaces of side outlets participate in heat exchange with the cooling water, which expands the heat transfer areas and heightens cooling efficiency. (2) The part of the crossflow exhausted from the side outlets mixed with upstream crossflow in the downstream cooling water declines, the proportion of jet flow increases, and the cooling effect on the heat sink increases. Therefore, the temperature of the cooling water downstream declines and reduces the discrepancy in the cooling water temperature upstream and downstream; the temperature distribution of the heat sink becomes gradually uniform along the X direction.

The Nusselt number (\overline{Nu}) is important for evaluating heat transfer performance. The cooling capacity of different models can be compared on the basis of this parameter. \overline{Nu} is calculated by

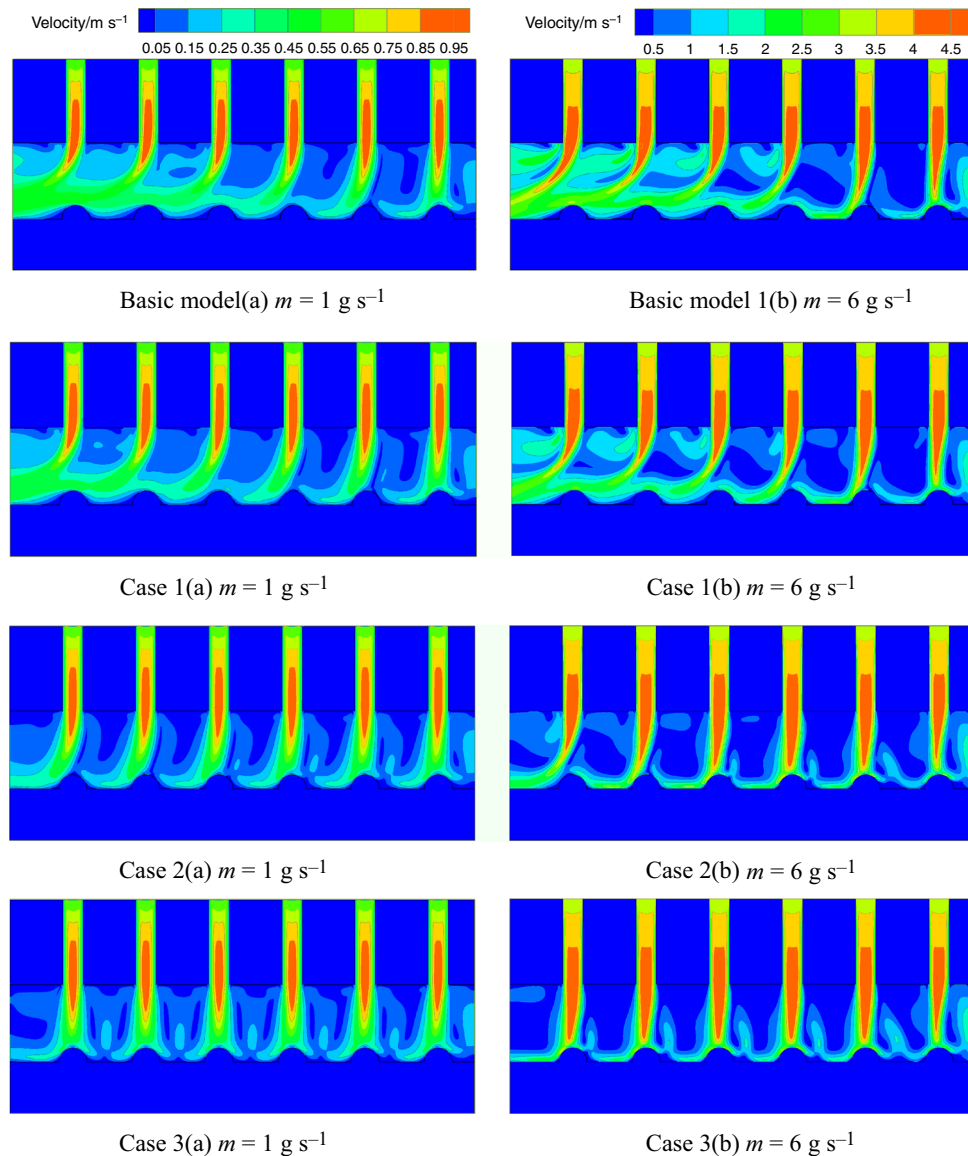


Fig. 6 Velocity distribution on symmetry plane of MHSIJD with different sizes of side outlets

$$\overline{Nu} = \frac{\overline{hd}}{k_f} \quad (7)$$

where

$$h = \frac{\hat{q}}{T_w - \overline{T}_f} \quad (8)$$

The \overline{Nu} of different structures are presented in Fig. 9 and demonstrate a growth trend with increasing velocity. The \overline{Nu} of any compared models is larger than the basic model, cooling capacity can be increased by 1.48–17.51%. A lower average temperature on the cooled surface of the former elucidates these phenomena.

Electronic chips cannot function normally beyond a certain tolerated temperature range; as such, the maximum

temperature on the cooled surface is another major criterion for evaluating microchannel heat sink performance. The maximum temperature on the cooled surface of any compared models is smaller than the basic model as shown in Fig. 10. The drift phenomenon in the compared model is weak, and the temperature of the cooling temperature is lower.

Analysis of resistance characteristics

The MHS can only be considered a reasonable design when controlling the pump consumption within acceptable limits. Usually, the flow resistance represents external pump consumption; in other words, flow resistance determines

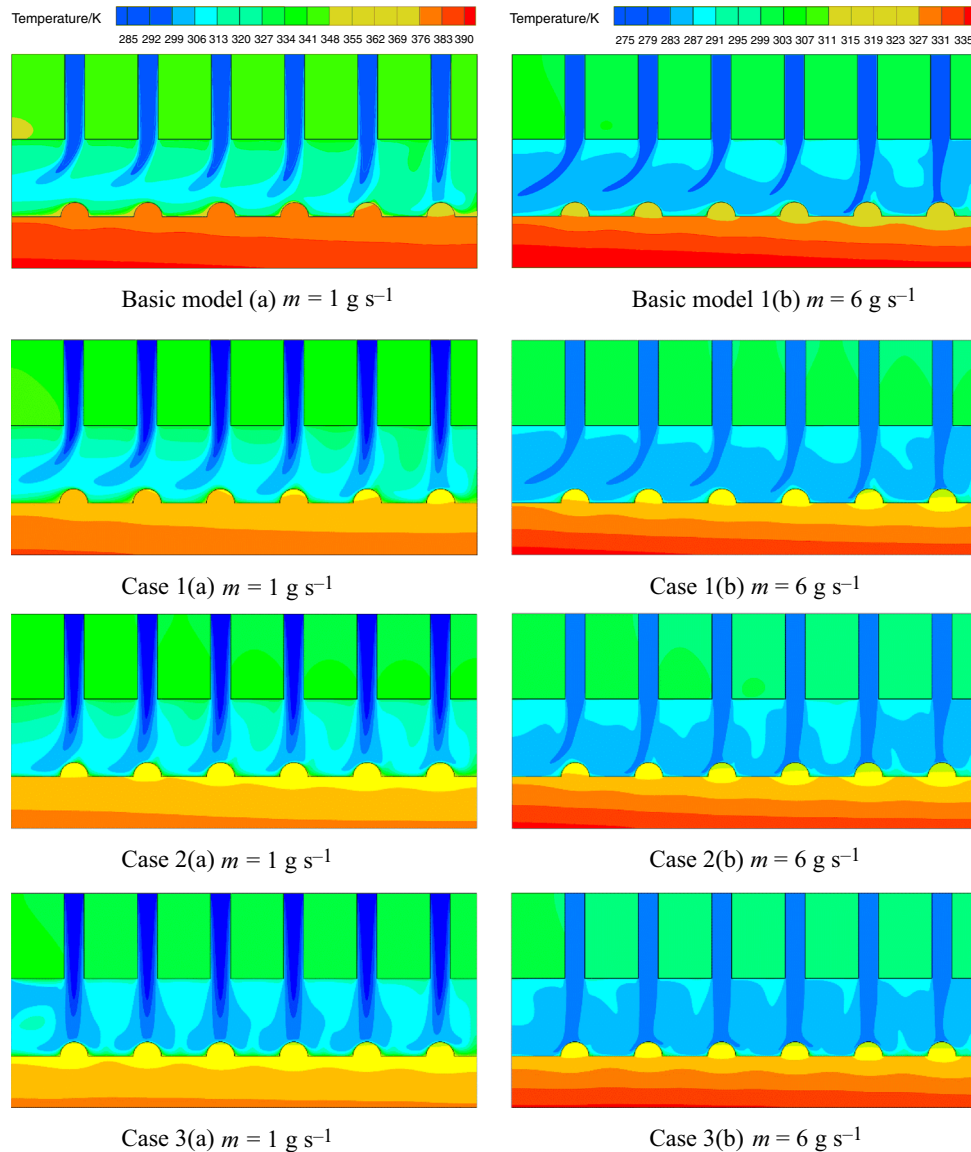


Fig. 7 Temperature distribution on symmetry plane of MHSIJD with different sizes of side outlets

the feasibility of the MHS. The pressure drop is used to measure flow resistance, calculated by

$$\Delta P = P_{\text{in}} - P_{\text{out}} \quad (9)$$

where P_{in} is the relative static pressure of the nozzle inlet farthest from the outlet, and P_{out} is the relative static pressure of the main outlet.

Compared with the basic model, the compared model contains more outlets, which causes earlier drainage, less water in the channel, a slower flow rate, and a smaller pressure drop; see Fig. 11. When the mass flow rate is 1 g s^{-1} , the pressure drop values of all models are nearly the same. As the mass flow rate increases, the flow resistance of each model increases, the pressure drop increases, and the rate of increase declines with an increase in the side

outlet area. As the side outlets area increases, more crossflow can flow out in time. This causes the fluid velocity in the channel to decrease, resulting in a reduced pressure drop. The pressure drop across the models varies, and this difference becomes more pronounced as mass flow increases; as the mass flow rate increases, the flow resistance in the microchannel increases sharply, and the pressure relief effect of the side outlet is reflected gradually. In the mass flow rate range of $1\text{--}6 \text{ g s}^{-1}$, the pressure drop can be reduced by 2.48–22.39%.

Analysis of overall performance

Heat transfer performance and resistance characteristics are evaluation indices of MHS. Therefore, the thermal

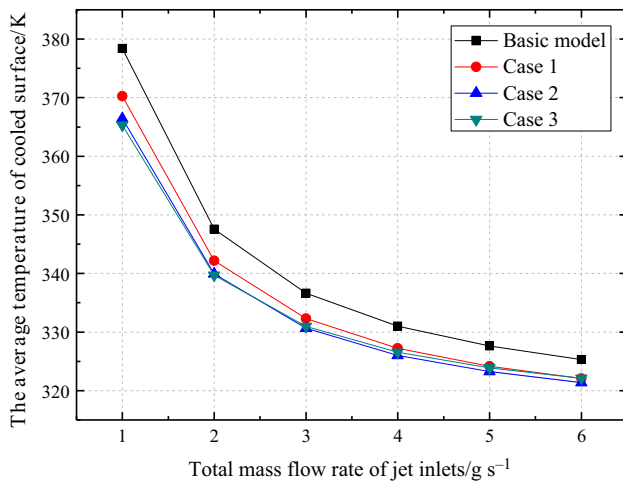


Fig. 8 Average temperature of cooled surface in different models

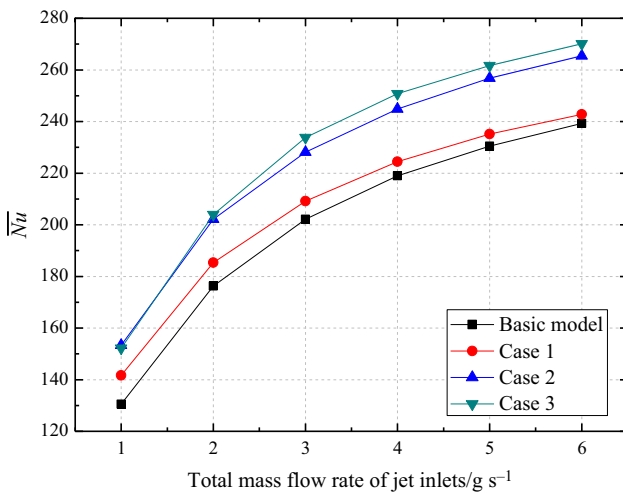


Fig. 9 Average Nusselt number in different models

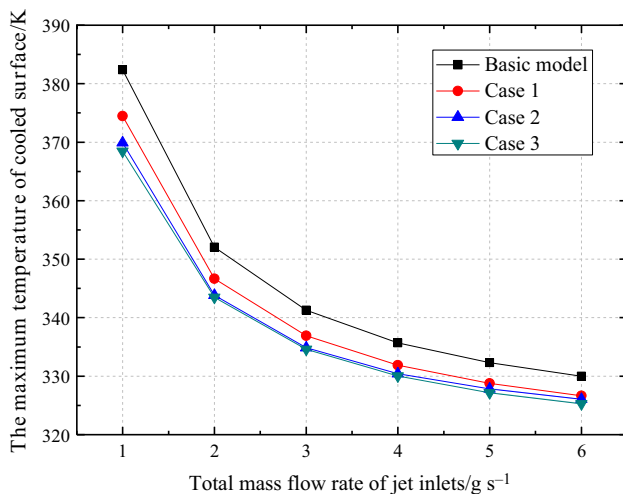


Fig. 10 Maximum temperature of cooled surface

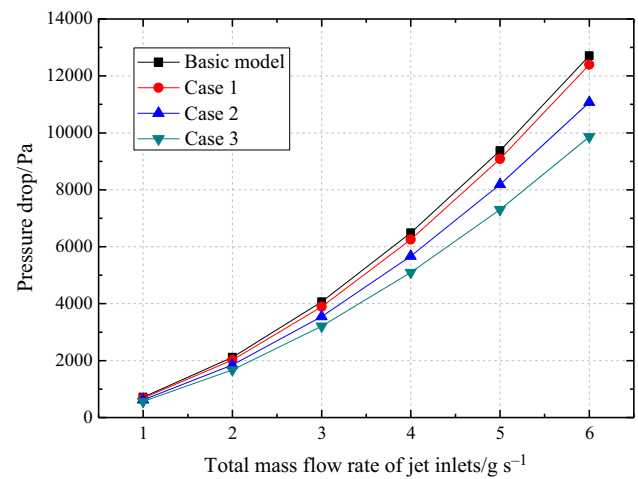


Fig. 11 Pressure drop in different models

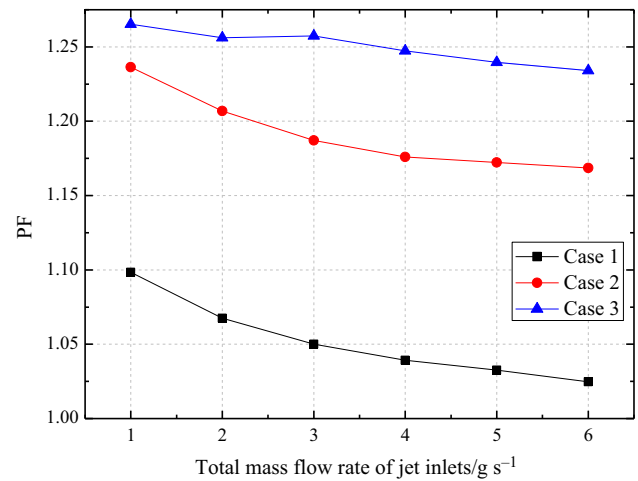


Fig. 12 PF in different models

performance and power consumption of the MHS should be considered collectively. In the present study, a dimensionless parameter PF (performance factor) [27] is taken as a comprehensive performance evaluation index for the MHS, defined as follows:

$$PF = \left(\frac{Nu}{Nu_0} \right) / \left(\frac{\Delta P}{\Delta P_0} \right)^{\frac{1}{3}} \quad (10)$$

where \overline{Nu} , ΔP , and \overline{Nu}_0 , ΔP_0 represent the Nusselt number and pressure drop of the compared model and basic model, respectively.

Figure 12 shows the overall performance of each model. At a given mass flow rate, the larger the side outlet area, the better the overall performance. In this case, the larger the side exit area, the higher the cooling efficiency and the smaller the power consumption. With an increase in mass flow, the comprehensive performance of each model tends

to be consistent. And the PF number reaches the maximum value at a mass flow rate of 1 g s^{-1} , when the height of microchannel side outlet is 0.6 mm. As shown in Fig. 12, at a given mass flow rate, the larger the side outlet area, the better the overall performance. However, if the side outlets surfaces continue to increase, the PF may keep rising, but the growth trend will slow down.

Future discussion

To alleviate the drift phenomenon in MHSIJD, a new MHSIJD model with side outlets was proposed in this study. Computational fluid dynamics simulation methodology with RNG $k\text{-}\varepsilon$ turbulence model was used to investigate the performance of an MHSIJD with side outlets. However, the number of models in this paper is limited. In the future work, we can analyze shape and arrangement of side outlets to obtain a better performance. In addition, we can study the characteristics of MHSIJD with side outlets under different working conditions to explore the applicability for cooling medium. More importantly, experimental investigations and optimization results should be performed for such kind of microchannel heat sink later on.

Conclusions

To improve the cooling capacity of the MHS, the effects of side outlets on thermal capability, pump consumption, and overall performance are simulated numerically. According to our findings, the following conclusions can be drawn:

1. The average temperature of hot surfaces with side outlets is higher than in the basic model, and the \overline{Nu} numbers is larger. Some parts of the crossflow escape from the side outlets, which alleviates the drift phenomenon. In addition, the portion of the inner walls of the side outlets that participate in heat exchange expand the heat transfer surface area. Some parameters of all structures exhibit a similar trend of increasing with an increase in the mass flow rate, average temperature of the cooled surface, and \overline{Nu} numbers; essentially, the larger the flow rate, the faster the heat can be removed. In the mass flow rate range of 1–6 g/s, heat transfer capacity can be increased by 1.48–17.51%
2. The pressure drop in MHSIJD with side outlets is lower than in the basic model and shows a tendency for the pressure drop to decline with an increase in the side outlets' area. The larger the side outlets, the lower the crossflow in the channel, which causes a lower pressure

drop. Under mass flow rate from 1 to 6 g/s, the pressure drop can be reduced by 2.48–22.39%.

3. The overall performance of the compared model is better than the basic model, and the performance is enhanced as the side outlets' area increases. As the side outlets' area increases, heat transfer is enhanced and pump consumption is reduced; thus, overall performance improves naturally. The PF number reaches the maximum value at a mass flow rate of 1 g/s, when the height of microchannel side outlet is 0.6 mm. However, with an increase in the mass flow rate, the difference in overall performance between the basic model and compared model declines. When the jet impact velocity is large, dominant heat dissipation is no longer microchannel heat dissipation but rather jet heat dissipation. In summary, adding side outlets can greatly improve fluid flow and heat transfer in MHSIJD. Augmenting the sizes of side outlets is an effective way to enhance heat transfer in MHS.

Acknowledgements This study is financially supported by the National Natural Science Foundation of China (Grant No. 51778511), the Hubei Provincial Natural Science Foundation of China (Grant No. 2018CFA029), and the Key Project of ESI Discipline Development of Wuhan University of Technology (WUT Grant No. 2017001).

References

1. Guo ZY. The frontier of international heat transfer research—fine-scale heat transfer. *Adv Mech.* 2000;30(1):1–6.
2. Dewan A, Srivastava P. A review of heat transfer enhancement through flow disruption in a microchannel. *J Therm Sci.* 2015;24(3):203–14.
3. Liou TM, Wei TC, Wang CS. Investigation of nanofluids on heat transfer enhancement in a louvered microchannel with lattice Boltzmann method. *J Therm Anal Calorim.* 2019;135(1):751–62.
4. Tuckerman DB, Pease RFW. High-performance heat sinking for VLSI. *IEEE Electron Device Lett.* 1981;2(5):126–9.
5. Drummond KP, Doosan B, Sinanis MD, Janes DB, Peroulis D, Weibel JA, Garimella SV. Characterization of hierarchical manifold microchannel heat sink arrays under simultaneous background and hotspot heating conditions. *Int J Heat Mass Transf.* 2018;126:1289–301.
6. Li P, Luo Y, Zhang D, Xie YH. Flow and heat transfer characteristics and optimization study on the water-cooled microchannel heat sinks with dimple and pin-fin. *Int J Heat Mass Transf.* 2018;119:152–62.
7. Alipour Lalami A, Hassanzadeh Afrouzi H, Moshfegh A. Investigation of MHD effect on nanofluid heat transfer in microchannels. *J Therm Anal Calorim.* 2019;136(5):1959–75.
8. Manay E, Mandev E. Experimental investigation of mixed convection heat transfer of nanofluids in a circular microchannel with different inclination angles. *J Therm Anal Calorim.* 2019;135(2):887–900. <https://doi.org/10.1007/s10973-018-7463-9>.
9. Khodabandeh E, Rozati SA, Joshaghani M, Akbari OA, Akbari S, Toghraie D. Thermal performance improvement in water nanofluid/GNP-SDBS in novel design of double-layer microchannel

- heat sink with sinusoidal cavities and rectangular ribs. *J Therm Anal Calorim.* 2019;136:1333–45.
10. Guthrie DGP, Torabi M, Karimi N. Energetic and entropic analyses of double-diffusive, forced convection heat and mass transfer in microreactors assisted with nanofluid. *J Therm Anal Calorim.* 2019;137(2):637–58. <https://doi.org/10.1007/s10973-018-7959-3>.
 11. Toghraie D, Abdollah MMD, Pourfattah F, Akbari OA, Ruhani B. Numerical investigation of flow and heat transfer characteristics in smooth, sinusoidal and zigzag-shaped microchannel with and without nanofluid. *J Therm Anal Calorim.* 2017;131(5):1–10.
 12. Liou TM, Wei TC, Wang CS. Investigation of nanofluids on heat transfer enhancement in a louvered microchannel with lattice Boltzmann method. *J Therm Anal Calorim.* 2019;135(1):751–62.
 13. Heydari A, Akbari OA, Safaei MR, Derakhshani M, Alrashed AAAA, Mashayekhi R, Shabani GAS, Zarringhalam M, Nguyen TK. The effect of attack angle of triangular ribs on heat transfer of nanofluids in a microchannel. *J Therm Anal Calorim.* 2018;131(3):2893–913.
 14. Akbari OA, Khodabandeh E, Kahbandeh F, Toghraie D, Khalili M. Numerical investigation of heat transfer of nanofluid flow through a microchannel with heat sinks and sinusoidal cavities by using novel nozzle structure. *J Therm Anal Calorim.* 2019. <https://doi.org/10.1007/s10973-019-08227-3>.
 15. Mohammadi M, Abadeh A, Reza NF, Mohammad PF. An optimization of heat transfer of nanofluid flow in a helically coiled pipe using Taguchi method. *J Therm Anal Calorim.* 2019. <https://doi.org/10.1007/s10973-019-08167-y>.
 16. Abazar A, Majid M, Mohammad PF. Experimental investigation on heat transfer enhancement for a ferrofluid in a helically coiled pipe under constant magnetic field. *J Therm Anal Calorim.* 2018. <https://doi.org/10.1007/s10973-018-7478-2>.
 17. Li J, Peterson GP, Cheng P. Three-dimensional analysis of heat transfer in a micro-heat sink with single phase flow. *Int J Heat Mass Transf.* 2004;47(19):4215–31.
 18. Wu HY, Cheng P. An experimental study of convective heat transfer in silicon microchannels with different surface conditions. *Int J Heat Mass Transf.* 2003;46(14):2547–56.
 19. Li Z, Tao WQ, He YL. A numerical study of laminar convective heat transfer in microchannel with non-circular cross-section. *Int J Therm Sci.* 2006;45(12):1140–8.
 20. Chen Y, Zhang C, Shi M, Wu J. Three-dimensional numerical simulation of heat and fluid flow in noncircular microchannel heat sinks. *Int Commun Heat Mass Transf.* 2009;36(9):917–20.
 21. Gunnasegaran P, Mohammed HA, Shuaib NH, Saidur R. The effect of geometrical parameters on heat transfer characteristics of microchannels heat sink with different shapes. *Int Commun Heat Mass Transf.* 2010;37(8):1078–86.
 22. Wang H, Chen Z, Gao J. Influence of geometric parameters on flow and heat transfer performance of micro-channel heat sinks. *Appl Therm Eng.* 2016;107:870–9.
 23. Xie XL, Liu ZJ, He YL, Tao WQ. Numerical study of laminar heat transfer and pressure drop characteristics in a water-cooled minichannel heat sink. *Appl Therm Eng.* 2009;29(1):64–74.
 24. Cao H, Chen G. Optimization design of microchannel heat sink geometry for high power laser mirror. *Appl Therm Eng.* 2010;30(13):1644–51.
 25. Utriainen E, Sundén B. Numerical analysis of a primary surface trapezoidal cross wavy duct. *Int J Numer Methods Heat Fluid Flow.* 2000;10(6):634–48.
 26. Mohammed HA, Gunnasegaran P, Shuaib NH. Numerical simulation of heat transfer enhancement in wavy microchannel heat sink. *Int Commun Heat Mass Transf.* 2011;38(1):63–8.
 27. Gong L, Kota K, Tao W, Joshi Y. Parametric numerical study of flow and heat transfer in microchannels with wavy walls. *J Heat Transf Trans ASME.* 2011;133(5):746.
 28. Lee DY, Vafai K. Comparative analysis of jet impingement and microchannel cooling for high heat flux applications. *Int J Heat Mass Transf.* 1999;42(9):1555–68.
 29. Ming TZ, Ding Y, Gui JL, Tao YX. Transient thermal behavior of a microchannel heat sink with multiple impinging jets. *J Zhejiang University Science A.* 2015;16(11):894–909.
 30. Sung MK, Mudawar I. Single-phase and two-phase cooling using hybrid micro-channel/slot-jet module. *Int J Heat Mass Transf.* 2008;51(15):3825–39.
 31. Sung MK, Mudawar I. Effects of jet pattern on two-phase performance of hybrid micro-channel/micro-circular-jet-impingement thermal management scheme. *Int J Heat Mass Transf.* 2009;52(13):3364–72.
 32. Sung MK, Mudawar I. CHF determination for high-heat flux phase change cooling system incorporating both micro-channel flow and jet impingement. *Int J Heat Mass Transf.* 2009;52(3):610–9.
 33. Jang SP, Kim SJ, Paik KW. Experimental investigation of thermal characteristics for a microchannel heat sink subject to an impinging jet, using a micro-thermal sensor array. *Sens Actuators, A.* 2003;105(2):211–24.
 34. Shafeie H, Abouali O, Jafarpur K, Ahmadi G. Numerical study of heat transfer performance of single-phase heat sinks with micro pin-fin structures. *Appl Therm Eng.* 2013;58(1–2):68–76.
 35. Mishra C, Peles Y. Laminar flow across a bank of low aspect ratio micro pin fins. *J Fluids Eng.* 2005;127(3):419–30.
 36. Jin Z, Huang S, Liang G, Huang Z. Numerical study and optimizing on micro square pin-fin heat sink for electronic cooling. *Appl Therm Eng.* 2016;93:1347–59.
 37. Hua J, Li G, Zhao X, Li Q, Hu J. Study on the flow resistance performance of fluid cross various shapes of micro-scale pin fin. *Appl Therm Eng.* 2016;107:768–75.
 38. Hong F, Cheng P. Three dimensional numerical analyses and optimization of offset strip-fin microchannel heat sinks. *Int Commun Heat Mass Transf.* 2009;36(7):651–6.
 39. Moores KA, Kim J, Joshi YK. Heat transfer and fluid flow in shrouded pin fin arrays with and without tip clearance. *Int J Heat Mass Transf.* 2009;52(25):5978–89.
 40. Reyes M, Arias JR, Velazquez A, Vega JM. Experimental study of heat transfer and pressure drop in micro-channel based heat sinks with tip clearance. *Appl Therm Eng.* 2011;31(5):887–93.
 41. Mei D, Lou X, Miao Q, Yao Z, Liang L, Chen Z. Effect of tip clearance on the heat transfer and pressure drop performance in the micro-reactor with micro-pin-fin arrays at low Reynolds number. *Int J Heat Mass Transf.* 2014;70(2):709–18.
 42. Liu W, Liu P, Wang JB, Zheng NB, Liu ZC. Exergy destruction minimization: a principle to convective heat transfer enhancement. *Int J Heat Mass Transf.* 2018;122:11–21.
 43. Xu M, Lu H, Gong L, Chai JC, Duan X. Parametric numerical study of the flow and heat transfer in microchannel with dimples. *Int Commun Heat Mass Transf.* 2016;76(5):348–57.
 44. Lan J, Xie Y, Zhang D. Flow and heat transfer in microchannels with dimples and protrusions. *J Heat Transf Trans ASME.* 2012;134(2):021901.
 45. Bi C, Tang GH, Tao WQ. Heat transfer enhancement in mini-channel heat sinks with dimples and cylindrical grooves. *Appl Therm Eng.* 2013;55(1–2):121–32.
 46. Li P, Zhang D, Xie Y. Heat transfer and flow analysis of Al₂O₃-water nanofluids in microchannel with dimple and protrusion. *Int J Heat Mass Transf.* 2014;73(73):456–67.
 47. Li P, Xie Y, Zhang D, Xie G. Heat transfer enhancement and entropy generation of nanofluids laminar convection in microchannels with flow control devices. *Entropy.* 2016;18(4):134.

48. Li P, Zhang D, Xie Y, Xie G. Flow structure and heat transfer of non-Newtonian fluids in microchannel heat sinks with dimples and protrusions. *Appl Therm Eng.* 2016;94:50–8.
49. Chang SW, Chiou SF, Chang SF. Heat transfer of impinging jet array over concave-dimpled surface with applications to cooling of electronic chipsets. *Exp Thermal Fluid Sci.* 2007;31(7):625–40.
50. Kanokjaruvijit K, Martinezbotas RF. Parametric effects on heat transfer of impingement on dimpled surface. *J Turbomach.* 2005;127(2):77–88.
51. Huang X, Yang W, Ming T, Shen W, Yu X. Heat transfer enhancement on a microchannel heat sink with impinging jets and dimples. *Int J Heat Mass Transf.* 2017;112:113–24.
52. Ming T, Cai C, Yang W, Shen W, Feng W, Zhou N. optimization of dimples in microchannel heat sink with impinging jets-part B: the influences of dimple height and arrangement. *J Therm Sci.* 2018;14:1–10.
53. Ming T, Cai C, Yang W, Shen W, Gan T. Optimization of dimples in microchannel heat sink with impinging jets-part A: mathematical model and the influence of dimple radius. *J Therm Sci.* 2018;27(3):195–202.
54. Ming T, Peng C, Gui J, Tao Y. Analysis on the hydraulic and thermal performances of a microchannel heat sink with extended-nozzle impinging jets. *Heat Transf Res.* 2016;48(10):893–914.
55. Li CG, Zhou JM. Experimental and numerical simulation study of heat transfer due to confined impinging circular jet. *Chem Eng Technol.* 2010;30(11):1355–61.
56. El-Gabry LA, Kaminski DA. Experimental investigation of local heat transfer distribution on smooth and roughened surfaces under an array of angled impinging jets. *J Turbomach Trans ASME.* 2005;127(3):532–44. <https://doi.org/10.1115/1.1861918>.

Publisher's Note Springer Nature remains neutral with regard to jurisdictional claims in published maps and institutional affiliations.